Korean J. Chem. Eng., 37(9), 1507-1514 (2020)
DOI: 10.1007/s11814-020-0560-z

pISSN: 0256-1115
eISSN: 1975-7220

Modified blue TiO_2 nanostructures for efficient photo-oxidative removal of harmful NO_x gases

Hao Huy Nguyen*, Gobinda Gyawali,†, Adriana Martinez-Oviedo***, Hoang Phuc Nguyen****, and Soo Wohn Lee***,†**

*Faculty of Applied Sciences, Ton Duc Thang University, Ho Chi Minh City, Vietnam
**Department of Fusion Science and Technology, Sun Moon University, Asan 31460, Korea
***Department of Environmental and Bio-chemical Engineering, Sun Moon University, Asan 31460, Korea
****Research Center for Eco-Multifunctional Nano Materials, Sun Moon University, Asan 31460, Korea
(*Received 21 January 2020 • Revised 22 April 2020 • Accepted 27 April 2020*)

Abstract−Blue TiO_2 nanostructures were produced via Lithium/ethylenediamine (Li/EDA) reduction method and applied for photo-oxidative removal of harmful NO_x gases under simulated solar light irradiation. Blue TiO_2 possesses some unique physicochemical properties such as enhanced visible-light absorption, superficial defects or oxygen vacancies, and the evolution of Ti^{3+} species. Moreover, the photoluminescence spectra (PL) revealed the efficient separation of photoinduced electron-hole pairs in the modified blue TiO_2 nanostructures, enhancing their photocatalytic activities. The results indicated that the blue TiO_2 nanostructures exhibited the highest performance towards photo-oxidation of NO_x gases, with an efficiency of 72.6% under simulated solar light irradiation.

Keywords: Photocatalyst, Blue TiO_2, Oxygen Vacancy, NO_x Gas

INTRODUCTION

Air pollution is fully acknowledged as a major environmental problem owing to its direct influence on the ecosystem and all living organisms. Exhaust gases after burning fossil fuels are the main contributors to air pollution. These gases are mainly composed of carbon monoxide (CO), carbon dioxide (CO_2), sulfur dioxide (SO_2), and the different forms of nitrogen oxides (NO_x) [1]. Among them, NO_x, which refers mainly to a mixture of NO and NO_2, has been paid much attention to scientists due to adverse effects on the environment and living organisms. The emission of NO_x in the atmosphere is responsible for serious environmental concerns, including acid rain, photochemical smog, and stratospheric ozone depletion [1-3]. Moreover, NO_x gases affect the respiratory system, causing inflammation in the respiratory tracks and lungs. Also, long-term exposure to NO_x can reduce lung function and increase the risk of respiratory disease [4,5]. In addition, NO_x gas has revealed that it can have a harmful effect on the physiological metabolism and content of secondary metabolites in plants, causing oxidative damage to nucleic acids, proteins, lipids, aquatic, and terrestrial ecosystems [6]. Due to various hazardous impacts related to NO_x pollution, it is necessary to disinfect or control the released NO_x gases. Currently, one of the effective methods applied to NO_x abatement is preventing the formation of NO_x in the air by using a low-level nitrogen fuel such as natural gas instead of coal or heavy oil [1]. However, natural gas cannot replace high nitrogen fuels in all situations.

Decomposition of the NO_x gas by using a selective non-catalytic reduction process could be an option. In this process, ammonia (NH_3) or urea (NH_2CONH_2) is injected into the firebox of the boiler at high temperature to react with the nitrogen oxides formed in the combustion process [7,8]. Because of the chemical redox reaction, nitrogen gas is produced instead of NO_x based on the following possible reactions:

$$NH_2CONH_2+H_2O\rightarrow 2NH_3+CO_2$$
$$4NH_3+4NO+O_2\rightarrow 4N_2+6H_2O$$
$$4NH_3+2NO_2+O_2\rightarrow 3N_2+6H_2O$$

Although the selective non-catalytic reduction method has many advantages, such as relatively simple installation, low investment costs, low energy use, and little space occupied, the process has some drawbacks too. The requirement of high temperature, the optimum reaction temperature in a narrow range, and secondary emission of gases like CO_2 and NH_3 are challenging. These negatives are limiting commercial applications of the selective non-catalytic reduction process.

In the last decades, one of the promising techniques to control environmental pollution is the use of photocatalysts, which can efficiently convert these pollutants into harmless products by utilizing green solar energy [9]. TiO_2 is a typical standard photocatalyst because of its unique properties, such as high photo-responsivity, nontoxic, and stable photocatalyst. Unfortunately, TiO_2 can only be excited under ultraviolet light (UV) to be active for photocatalysis due to its relatively larger band gap energy (~3.2 eV for anatase phase and ~3.0 eV of rutile phase) [10]. Thus, these drawbacks of pristine TiO_2 prevent the effective utilization of sunlight. Sunlight comprises about 5% of the UV spectrum, whereas the remaining major portion of the solar spectrum is comprised of the visible spectrum. Therefore, it is necessary to reduce the band gap energy of TiO_2 so

†To whom correspondence should be addressed.
E-mail: ggobinda@sunmoon.ac.kr, swlee@sunmoon.ac.kr

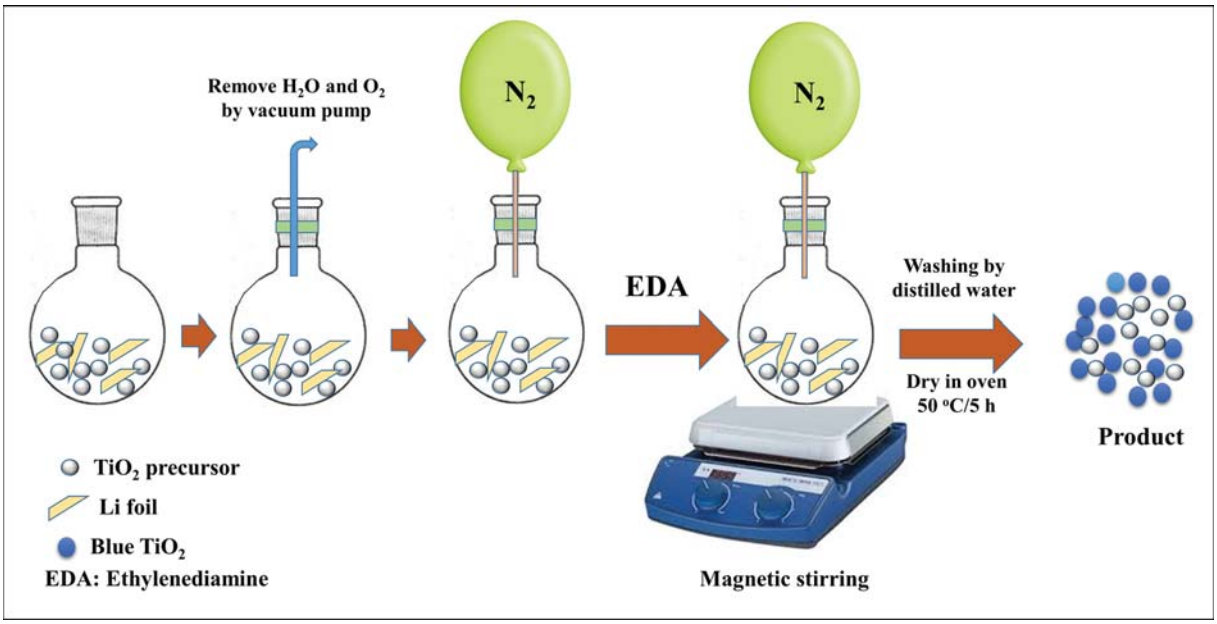

Fig. 1. Synthesis process of b-TiO_2 and n/b-TiO_2.

that the photo-responsive ability can be tuned towards visible light. Blue TiO_2 or surface-disordered TiO_2, which is composed of a thin disordered shell and a lattice core, has received much attention owing to its visible light-responsive characteristics and enhanced photocatalytic activities [11]. Zhang et al. [11] indicated a strong redshift in the absorption to the visible light region of the blue TiO_2. Similarly, Adriana et al. [9] reported broad absorption at wavelengths up to 800 nm, whereas the precursor TiO_2 presents absorption only in the UV light. Moreover, the synthesis process of the blue TiO_2 produces superficial defects, including Ti^{3+} and oxygen vacancies, acting as barriers for the recombination of electron-hole pairs. In addition to the photocatalysis, the blue TiO_2 has also shown improved performance in the dye-sensitized solar cells [12,13], Lithium-ion rechargeable batteries [14], disinfection of freshwater algae [15], and supercapacitors [16,17]. However, a detailed study of surface disordered blue TiO_2 and their different nanostructures for the NO_x removal is still lacking. Hence, in this work, we report the investigation of the reduced blue TiO_2 materials for NO_x removal efficiencies.

EXPERIMENTAL

1. Materials

The precursor TiO_2-P25 (P25) (Degussa), Lithium foil (98%, Samchun Chemical), Ethylenediamine (98%, Sigma Aldrich), H_2SO_4 (Samchun Chemical), HCl (35%, Duksan), and NaOH (Sigma-Aldrich) were used to synthesize blue TiO_2 particles (b-TiO_2), nanostructured TiO_2 (n-TiO_2), and nanostructured blue TiO_2 (n/b-TiO_2).

2. Synthesis of the Reduced Forms of TiO_2

2-1. Synthesis of n-TiO_2

The n-TiO_2 was prepared via a microwave-assisted hydrothermal method as described in our previous work with a minor modification [12]. Briefly, a mixture of 0.5 g of P25 and 25 mL of 10 M NaOH was stirred gently for 30 min to form a suspension at room temperature. Then, the resulting suspension was transferred to a Teflon vessel reactor for the microwave hydrothermal process. The n-TiO_2 was formed in the microwave reaction system at 100 °C, 295 W, and 300 rpm for 4 h. After that, the n-TiO_2 was washed several times with double distilled water and 0.5 M HCl, finally dried in a freeze dryer (EYELA, FDU-2100) at −80 °C for 20 h. The nanostructured TiO_2 consisted of a mixture of nanoparticles, nanorods, nanotubes, and nanosheets as well.

2-2. Synthesis of b-TiO_2 and n/b-TiO_2

The reduced b-TiO_2 or n/b-TiO_2 were synthesized by reducing P25 or n-TiO_2 using Li/EDA as a reducing agent [9,11-13], according to the process demonstrated in Fig. 1. First, a mixture of 0.35 g of Li foil, 50 mL of EDA, and 0.5 g of precursor TiO_2 (P25 or n-TiO_2) was placed in a glass reactor filled full with nitrogen gas. Then, the mixture was stirred in the dark condition for six days. After that, the obtained product was neutralized by HCl and washed with distilled water and dried in an oven at 40 °C for 6 h. Finally, the powder was ground in a mortar to form b-TiO_2 or n/b-TiO_2.

3. Characterization

The crystal structures of all samples were identified by X-ray diffraction analysis, measured at 2θ angles from 5° to 70° using a monochromatized Cu-Kα (λ=1.54 Å) radiation. The morphologies, microstructures, and particle size of products were observed by high-resolution transmission electron microscopic technique (HRTEM, FEI, TitanTM 80-300). Photoluminescence (PL) spectra were measured using a photoluminescence spectrometer (FLS980, Edinburgh Instruments). X-ray photoelectron spectroscopy (XPS) was measured with an X-ray monochromator, XR5 Gun-500 μm, from Thermo-scientific Instruments. The light absorption ability and band gap values were analyzed by UV-Vis diffuse reflectance spectrophotometer (DRS, UV-Vis V-500, Jasco). The specific surface area of the samples was recorded by N_2 adsorption-desorption mea-

surement via Brunauer Emmett Teller (BET) method using a Micromeritics ASAP 2020. Raman spectroscopy (LabRAM HR 800, Horiba coupled with an Olympus BX41 optical microscope) was used to collect Raman spectra. The concentration of nitrate ions was analyzed by combustion ion chromatography (ICS 3000, Dionex).

4. Photocatalytic Measurement

The photocatalytic activity of the as-synthesized samples for NO_x removal was evaluated by a Horiba APNA-370 system according to the literature with a bit of modification [10]. The inlet gas flow was a mixture of NO_x gases with an initial concentration of 300 ppb of NO and 30 ppb of NO_2. A photocatalytic paste was prepared by mixing 0.05 g of the photocatalyst in 2 mL ethanol. The paste was then coated on a dish (diameter, d=5 cm), dried at room temperature and placed in the reactor. A 150 W commercial xenon arc lamp (Abet technologies, LSA-150) was used as a source of light. The experiments were conducted for 30 min in the dark, followed by simulated solar light irradiation for 60 min.

RESULTS AND DISCUSSION

1. X-ray Diffraction Analysis

Fig. 2 shows the XRD patterns of P25, b-TiO_2, n-TiO_2, and n/b-TiO_2. The diffraction peaks of P25 reveal a mixture of anatase (JCPDS No.21-1272) and rutile (JCPDS No.46-1238) phases. In

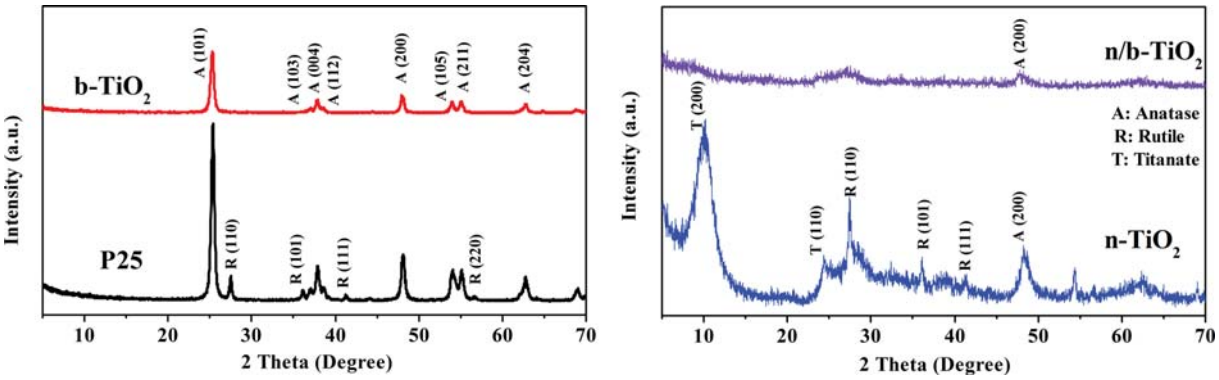

Fig. 2. XRD diffraction patterns of samples.

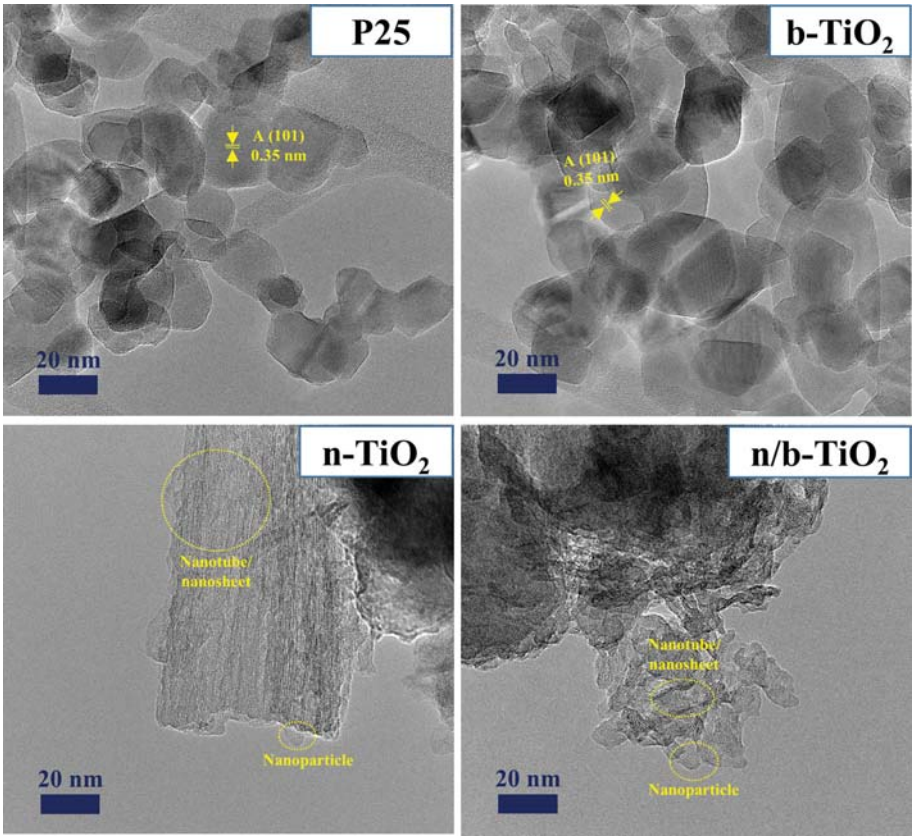

Fig. 3. HRTEM images of samples.

the b-TiO_2, the peaks corresponding to the rutile phase disappear, with just anatase phase remaining. In the nanostructured TiO_2, both anatase and rutile phases are present, which are distinctly represented by the appearance of anatase phase, A (200), and rutile phase, R (110), R (101), and R (111), peaks. However, all diffraction peaks of the rutile phase disappeared in the nanostructured blue TiO_2 (n/b-TiO_2). The absence of the rutile peaks in both b-TiO_2 and n/b-TiO_2 is due to the selective reduction of the rutile phase by Li/EDA reducing agent during the reaction. The possible mechanism to explain the selective reduction of the rutile phase, from a mixture of both rutile and anatase phases, may be due to the different protonation constants of these two phases against pH [11,13,15]. Following that, the anatase phase was stabilized in a super base Li/EDA environment, whereas the rutile phase was damaged easily into the amorphous phase. Due to this selective reduction phenomenon, the surface of b-TiO_2 and n/b-TiO_2 produced a disordered layer. Kim et al. [15] indicated that the disorder shell content has an effect on the coloring of the product, which changes from light blue to black depending on the percentage of the rutile phase in the precursor.

2. TEM Observation

Fig. 3 shows the HRTEM images of P25, b-TiO_2, n-TiO_2, and n/b-TiO_2. The P25 and b-TiO_2 consist of the spherical or oval shape of nanoparticles with a diameter ranging from 10 to 30 nm. The HRTEM image of P25 revealed the existence of the lattice fringes (101) corresponding to the anatase phase. The n-TiO_2 and n/b-TiO_2 are composed of a mixed form morphologies consisting of spherical nanoparticles, nanosheets as well as nanotubes. The presence of different morphological and structural variations could lead to create heterojunctions. It has been revealed from the studies [18, 19] that the presence of heterojunctions in the photocatalyst enhance the photocatalytic activities by effective separation of photoinduced electrons and holes.

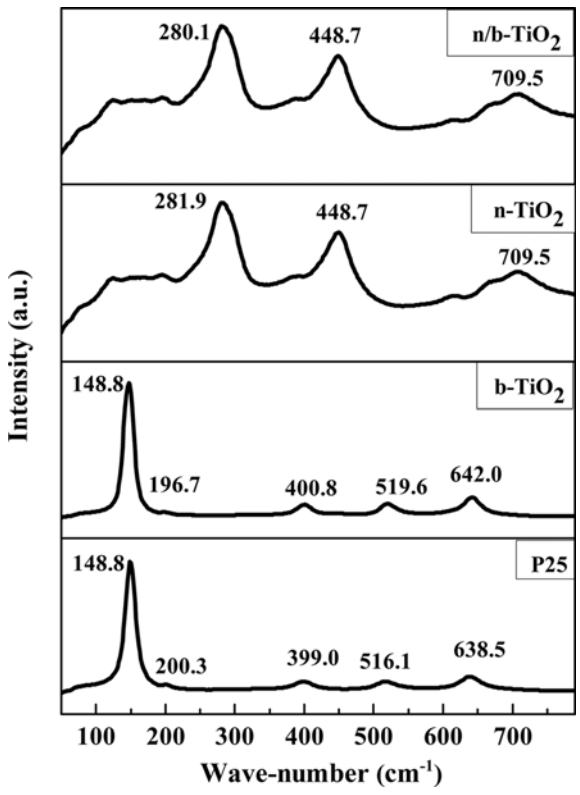

Fig. 4. Raman spectra of samples.

3. Raman Analysis

Fig. 4 shows the Raman spectra of samples. P25 exhibits five peaks of anatase phase located at 148.8, 200.3, 399.0, 516.1, and 638.5 cm^{-1}, which correspond to Eg, Eg, B1g, A1g, and E2g modes [20]. These peaks shift to 147.0, 196.7, 400.8, 519.6, and 642.0 cm^{-1} in b-TiO_2, respectively. The n-TiO_2 has three main Raman peaks at 281.9, 448.7, and 709.5 cm^{-1}. In the n/b-TiO_2, the peaks centered at 448.7 and 709.5 cm^{-1} remain at the same position as compared to the corresponding peak position in the n-TiO_2 sample. However, the peak at 281.9 cm^{-1} is shifted slightly towards the lower wavenumber at 280.1 cm^{-1} in the n/b-TiO_2. The shifting of Raman peaks in the reduced TiO_2 products might be due to the formation of disorder shell after Li/EDA reduction process. The disorder shell might have contributed to decrease in Raman peak intensities in b-TiO_2 and n/b-TiO_2 samples as compared to P25 and n-TiO_2 samples.

4. XPS Analysis

The surface chemistry, binding energy, and the changes of chemical and electronic states of elements of the prepared samples were investigated by XPS analysis. Fig. 5(a)-(d) show the deconvoluted XPS spectra of O 1s state of as-synthesized samples. The results indicate that the O 1s state of non-reduced samples (P25 and n-TiO_2) possess two different broad peaks with variable intensities. The peaks at 530.6 eV (P25) and 530.3 eV (n-TiO_2) can be ascribed to the lattice oxygen (O_L). Similarly, the deconvoluted peaks at 531.7 eV (P25) and 532.7 eV (n-TiO_2) are contributed by non-lattice oxygen or chemisorbed oxygen (O_C). On the other hand, an additional deconvoluted peak that appears at 530.6 eV is assigned to the oxygen vacancy (O_V) in the reduced blue TiO_2 samples, as shown in Fig. 5(c)-(d). The deconvoluted XPS spectra of Ti 2p state of the samples are shown in Fig. 5(e)-(h). Each deconvoluted Ti 2p spectrum of P25 and n-TiO_2 is composed of only two peaks corresponding to Ti^{4+} 2p3/2 and Ti^{4+} 2p1/2. Interestingly, the deconvoluted Ti 2p spectra of b-TiO_2 and n/b-TiO_2 samples exhibit two new peaks at 460.2 and 463.4 eV (b-TiO_2), and 459.6 and 462.4 eV (n/b-TiO_2), representing Ti^{3+} 2p3/2, and Ti^{3+} 2p1/2 states, respectively. Here, the experimental results confirm the formation of Ti^{3+} species and oxygen vacancies due to the selective reduction of the rutile phase of TiO_2 by Li/EDA.

5. Photoluminescence Spectra

The PL spectra were measured to analyze the recombination efficiency of photogenerated carriers, which is quantified by PL intensity. As shown in Fig. 6, the lower emission peak intensities in b-TiO_2 and n/b-TiO_2 indicate the lower recombination rate of photoelectrons and holes as compared to P25 and n-TiO_2 samples. The presence of Ti^{3+} species and oxygen vacancies are possible contributing factors to decrease PL intensities in the reduced b-TiO_2 and n/b-TiO_2 samples. These defects act as trapping centers for electrons and holes, thereby enhancing the separation of photogenerated charge carriers. Moreover, PL emission peaks intensities of n/b-TiO_2 are lower than that of b-TiO_2. This outcome is probably due to the formation of heterojunctions among spherical or oval nanoparticles,

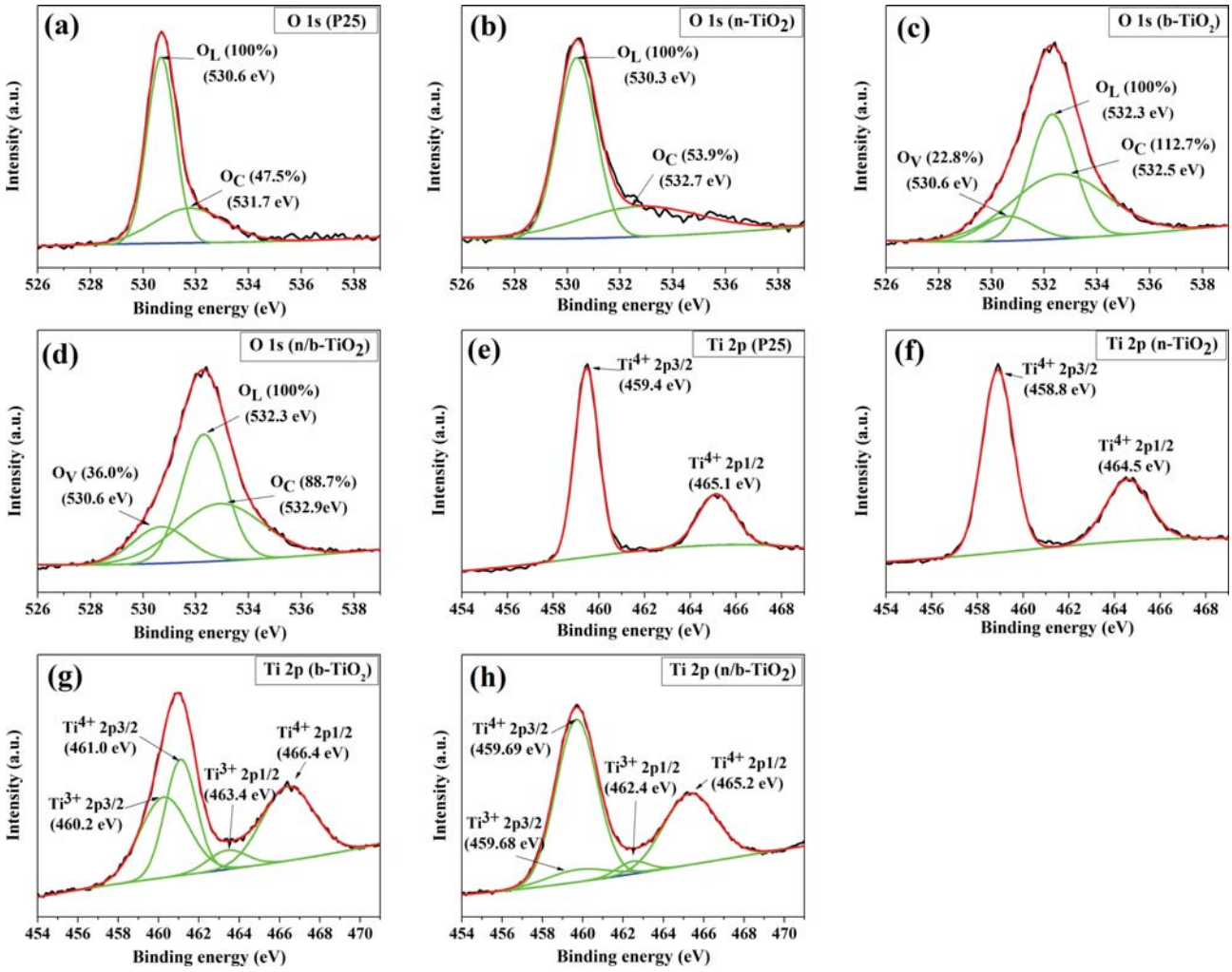

Fig. 5. X-ray photoelectron spectra of samples.

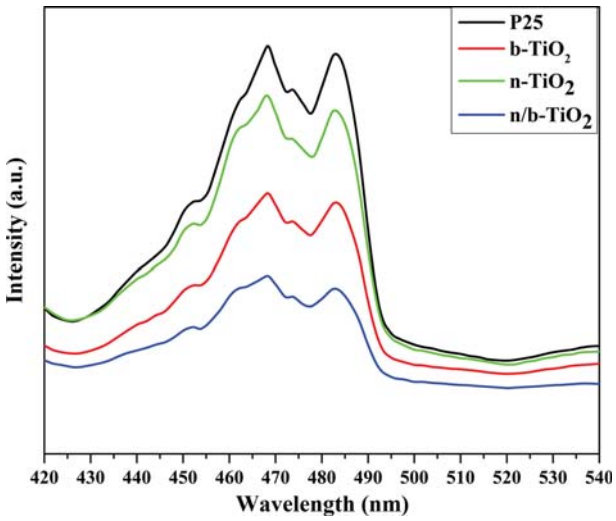

Fig. 6. Photoluminescence spectra of samples.

nanosheets, and nanotubes in n/b-TiO_2. As a result, photogenerated charge carriers spread through heterojunctions leading to efficient charge separation.

6. UV-Vis DRS Analysis

UV-Vis DRS was measured to investigate the photo-responsive abilities and band-gap energies of the samples, as shown in Fig. 7. The UV-Vis spectra of the reduced samples (b-TiO_2, and n/b-TiO_2) demonstrated a strong absorption in the visible region above 400 nm. However, P25 and n-TiO_2 samples show the light absorption in the UV region only. The existence of superficial defects, including Ti^{3+} and oxygen vacancies in b-TiO_2 and n/b-TiO_2 samples, are ascribed to this outcome. These defects may form the mid-gap states in the band-gap energy, which facilitates photoelectrons to excite and jump into the mid-gap stages even in the low energy visible light range. Moreover, it is interesting that the light absorption in the visible spectrum by b-TiO_2 and n/b-TiO_2 is gradually increased at higher wavelength, as depicted in Fig. 7(a). Particularly, the light absorption spectrum of n/b-TiO_2 indicates that from 600 to 800 nm wavelength, the absorbance is higher than the ultraviolet region. The band gap values of P25, n-TiO_2, b-TiO_2, and n/b-TiO_2, calculated by using the Kubelka-Munk method are 3.28, 3.45, 3.20, and 3.12 eV, respectively. Although the band gap values are relatively higher for the visible light to be absorbed by b-TiO_2 and n/b-TiO_2 samples,

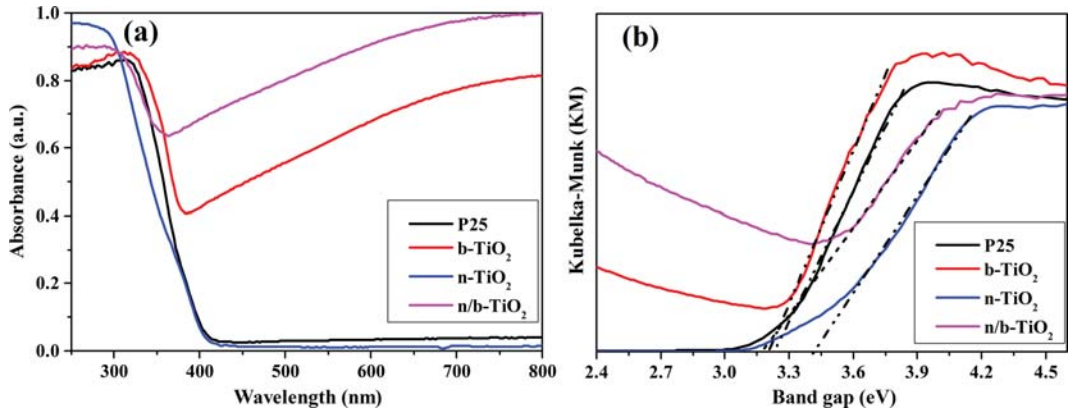

Fig. 7. UV-vis spectra (a) and band gap energy (b) of samples.

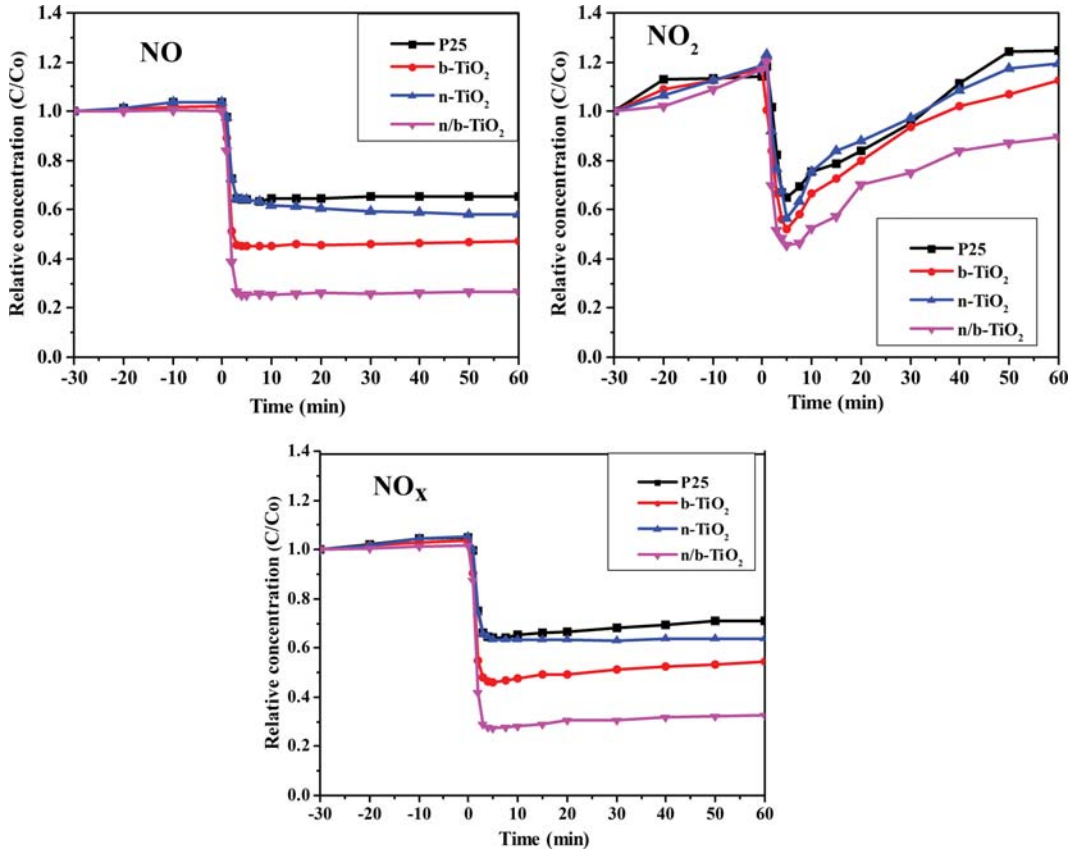

Fig. 8. Photocatalytic removal of NO_x.

the formation of mid-gap stages due to the existence of Ti^{3+} species is responsible for the outcome.

7. Photocatalytic Performance

The photocatalytic performance of P25, b-TiO_2, n-TiO_2, and n/b-TiO_2 was evaluated through the transformation of relative concentration (C/C_o) of NO and NO_2. The decrease in concentration of NO_x gases by different samples under simulated solar light is shown in Fig. 8. All samples show a decrease of NO_x concentration after the first 5 min of irradiation. Additionally, the reduced TiO_2 samples, b-TiO_2 and n/b-TiO_2, show better performance for NO_x removal efficiency, corresponding to 44.8% and 72.6%. Meanwhile, P25 and n-TiO_2 were able to decrease only 36.1% and 37.1% of the initial concentration. The comparative analysis of the NO_x removal efficiency, listed in Table 1, indicates that the material n/b-TiO_2 displays higher potential for the treatment of environmental pollution [21-26].

The possible mechanism is illustrated in Fig. 9. As TiO_2 is exposed with solar light, electrons in the valence band (VB) absorb photons to jump into the conduction band (CB) and leave behind holes. In VB, the holes react with hydroxyl ions (OH^-) from the water or

Table 1. Comparative study of the NO_x photo-oxidation efficiency of TiO_2 based photocatalysts

Samples	Experiment conditions	NO removal (%)	References
TiO_2/C	6 W UV lamp, 365 nm, 200 ppb NO, GHSV=16-98 h^{-1}	66	[21]
B-PCN	300 W halogen lamp (420-700 nm), 500 ppb NO, 0.2 g Catalyst	44.1	[22]
Ag/TiO_2	UV and visible light source, gas stream of NO/Ar	70	[23]
g-C_3N_4	Visible light, 500 ppb NO, 0.2 g catalyst	38.6	[24]
N-TiO_2/g-C_3N_4	Visible light, 0.2 g catalyst, 600 ppb NO	46.1	[25]
BiNPs-decorated-C_3N_4	Visible light, 500 ppb NO, 0.2 g catalyst	60.8	[24]
Pt-doped TiO_2	50 mg of catalyzer, uv and visible light, RH=70%, gas of NO, NO_2 and wet air	30	[26]
n/b-TiO_2	0.05 g of catalyst, 150 W commercial xenon arc lamp, 300 ppb NO	72.6	Our work

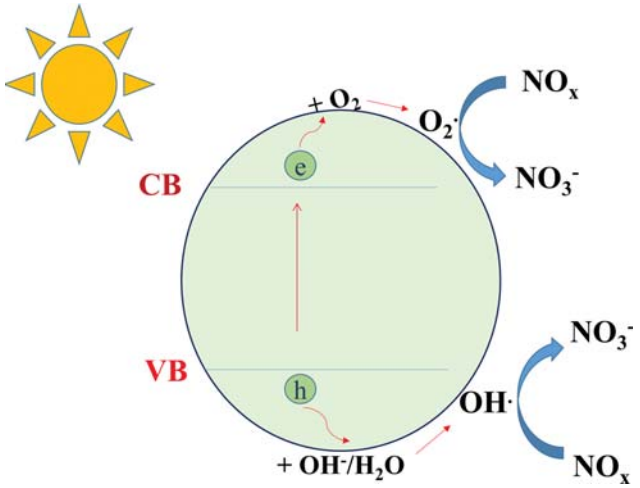

Fig. 9. Schematic mechanism of NO_x photo-oxidation.

inorganic substances to form hydroxyl radical ($OH^·$), which further combines with NO or NO_2 to produce a final product NO_3^- [9,27,28]. In CB, excited electrons reduce adsorbed oxygen to form superoxide ($O_2^{-·}$), then the superoxide reacts with NO_x to form NO_3^- [1,9,29].

Moreover, the oxidation of NO_x by the photoreactions was supported by the formation of nitrate ions that was analyzed by ion chromatography. The amount of nitrate ions adsorbed on the surface of P25 and TiO_2-p during 1 h of the irradiation corresponds to 0.69 and 3.23 mg/L; however, this number increases to 6.26 and 15.62 mg/L for b-P25 and n/b-TiO_2, respectively.

Clearly, the surface adsorbed substances (oxygen, water, organic chemicals) on the TiO_2 play an important role in photocatalysis because they serve as an electrolyte needed for the redox reaction promoted by the photoelectron-hole pairs [1]. The percentage of O_C on the surface of different TiO_2 samples obtained via deconvolution of XPS is 47.5% (P25), 53.9% (n-TiO_2), 112.7% (b-TiO_2), and 88.7% (n/b-TiO_2). The O_C percentage is consistent with the NO_x abatement induced by P25 (36.1%), n-TiO_2 (37.1%), b-TiO_2 (44.8%), and n/b-TiO_2 (72.6%). The improved photocatalytic activity of n/b-TiO_2 in comparison with b-TiO_2 may be due to the lower recombination rate of photogenerated charge carriers, which is evidenced from the PL spectra. Note that the NO_x removal performance of n/b-TiO_2 is higher than that of b-TiO_2. The possible reason might be due to the junction effect created from different crystal structures (nanoparticles, nanorods, nanotubes, and nanosheets) which exists in the n/b-TiO_2. According to Jiang et al. [25], the heterojunction might reduce the electron-hole recombination, thereby improving the utilization of these charge particles. In the n/b-TiO_2, the junction phase structure can make the photoelectrons transport among the different CBs of nanosheets, nanotubes, nanorods, and nanoparticles instead of jumping down to VBs and recombining with the holes. Therefore, the lifetime of electrons and holes in n/b-TiO_2 is expected to be prolonged more than the b-TiO_2, leading to enhancing photocatalytic activity. Furthermore, the formation of Ti^{3+} species, oxygen vacancies, at the blue photocatalyst also contributed to the photocatalytic activity of samples, causing better activity of blue TiO_2 than white TiO_2.

CONCLUSION

Blue TiO_2 nanomaterials were synthesized successfully by Li/EDA reduction method. The experimental results indicated the enhancement of light absorption in the visible region of the solar spectrum, reduction of band gap energy, formation of superficial defects such as oxygen vacancies and Ti^{3+} species, and the decrease of the recombination rate of e-h pairs in the reduced blue TiO_2 as compared to white TiO_2 (P25 and n-TiO_2). The experimental results also showed the enhancement of photo-oxidation of NO_x gases using the blue TiO_2 with the highest efficiency of the n/b-TiO_2 (72.6%).

ACKNOWLEDGEMENTS

This research was supported by the Global Research Laboratory Program (Grant Number: 2010-00339) of the National Research Foundation of Korea (NRF) funded by the Ministry of Education, Science, and Technology (MEST) of Korea.

REFERENCES

1. J. Ângelo, L. Andrade, L. M. Madeira and A. Mendes, *J. Environ. Manage.*, **129**, 522 (2013).
2. D. L. Mauzerall, B. Sultan, N. Kim and D. F. Bradford, *Atmos. Environ.*, **39**, 2851 (2005).
3. A. Chaloulakou, I. Mavroidis and I. Gavriil, *Atmos. Environ.*, **42**, 454 (2008).

4. T. Whyand, J. R. Hurst, M. Beckles and M. E. Caplin, *Respir. Res.*, **19**, 79 (2018).
5. B. Yacoubi, L. Samet, J. Bennaceur, A. Lamouchi and R. Chtourou, *Mater. Sci. Semicond. Process.*, **30**, 361 (2015).
6. S. Muneer and J. H. Lee, *Sci. Rep.*, **8**, 12291 (2018).
7. C. Locci, L. Vervisch, B. Farcy, P. Domingo and N. Perret, *Flow Turbulence Combust.*, **100**, 301 (2018).
8. S. Barman and L. Philip, *Environ. Sci. Technol.*, **40**, 1035 (2006).
9. A. Martinez-Oviedo, S. K. Ray, H. P. Nguyen and S. W. Lee, *J. Photochem. Photobiol. A Chem.*, **370**, 18 (2019).
10. H. P. Nguyen, M. Matsuoka, T. H. Kim and S. W. Lee, *J. Photochem. Photobiol. A Chem.*, **367**, 429 (2018).
11. K. Zhang, L. Wang, J. K. Kim, M. Ma, G. Veerappan, C. L. Lee, K. Kong, H. Lee and J. H. Park, *Energy Environ. Sci.*, **9**, 499 (2016).
12. H. H. Nguyen, G. Gyawali, T. H. Kim, S. Bin Humam and S. W. Lee, *Prog. Nat. Sci. Mater. Int.*, **28**, 548 (2018).
13. S. Bin Humam, H. H. Nguyen, C. Regmi, G. Gyawali, B. Joshi and S. W. Lee, *Ceram. Int.*, **45**, 4230 (2019).
14. Y. Yan, B. Hao, D. Wang, G. Chen, E. Markweg, A. Albrecht and P. Schaaf, *J. Mater. Chem. A*, **1**, 14507 (2013).
15. Y. Kim, H. M. Hwang, L. Wang, I. Kim, Y. Yoon and H. Lee, *Sci. Rep.*, **6**, 25212 (2016).
16. J. Yang, C. Zheng, P. Xiong, Y. Li and M. Wei, *J. Mater. Chem. A*, **2**, 19005 (2014).
17. X. Lu, G. Wang, T. Zhai, M. Yu, J. Gan, Y. Tong and Y. Li, *Nano Lett.*, **12**, 1690 (2012).
18. C. N. Ri, S. G. Kim, J. Y. Jong, S. N. Pak, S. C. Ri and J. H. Ri, *New J. Chem.*, **42**, 647 (2018).
19. J. Zhu, J. He, L. Hu and L. Da, *J. Solid State Chem.*, **276**, 104 (2019).
20. H. H. Nguyen, G. Gyawali and S. W. Lee, *J. Ceram. Process. Res.*, **17**, 409 (2016).
21. C. H. Ao and S. C. Lee, *Appl. Catal. B: Environ.*, **44**, 191 (2003).
22. J. Cao, J. Zhang, X. Dong, H. Fu, X. Zhang, X. Lv, Y. Li and G. Jiang, *Appl. Catal. B: Environ.*, **249**, 266 (2019).
23. M. Xu, Y. Wang, J. Geng and D. Jing, *Chem. Eng. J.*, **307**, 181 (2017).
24. G. Jiang, X. Li, M. Lan, T. Shen, X. Lv, F. Dong and S. Zhang, *Appl. Catal. B: Environ.*, **205**, 532 (2017).
25. G. Jiang, J. Cao, M. Chen, X. Zhang and F. Dong, *Appl. Surf. Sci.*, **458**, 77 (2018).
26. Y. Hu, X. Song, S. Jiang and C. Wei, *Chem. Eng. J.*, **274**, 102 (2015).
27. J. S. Dalton, P. A. Janes, N. G. Jones, J. A. Nicholson, K. R. Hallam and G. C. Allen, *Environ. Pollut.*, **120**, 415 (2002).
28. Q. L. Yu and H. J. H. Brouwers, *Appl. Catal. B: Environ.*, **92**, 454 (2009).
29. Y. Hu, X. Song, S. Jiang and C. Wei, *Chem. Eng. J.*, **274**, 102 (2015).